Geoscience Data Journal

WILEY

Geoscience Data Journal RMetS

DATA ARTICLE OPEN ACCESS

DCENT-I: A Globally Infilled Extension of the Dynamically Consistent ENsemble of Temperature Dataset

Duo Chan[1] | Steven C. Chan[2] | Joseph T. Siddons[2] | Archie Cable[2] | Agnieszka Faulkner[2] | Richard C. Cornes[2] | Elizabeth C. Kent[2] | Geoffrey Gebbie[3] | Peter Huybers[4]

[1]School of Ocean and Earth Science, University of Southampton, Southampton, UK | [2]National Oceanography Centre, Southampton, UK | [3]Physical Oceanography, Woods Hole Oceanographic Institution, Falmouth, Massachusetts, USA | [4]Earth and Planetary Sciences, Harvard University, Cambridge, Massachusetts, USA

Correspondence: Duo Chan (duo.chan@soton.ac.uk)

Received: 31 August 2025 | **Revised:** 10 December 2025 | **Accepted:** 22 December 2025

Keywords: climate change | coverage uncertainty | ENSO | infill | surface temperature

ABSTRACT

A spatially infilled Dynamically Consistent Ensemble of surface Temperature (DCENT-I) has been created by infilling land-air and sea-surface temperatures from DCENT using ordinary kriging with anisotropic and heterogeneous kernels. By incorporating air temperature anomalies over sea-ice areas, DCENT-I provides spatially complete monthly temperature fields at 5° resolution from 1850 to the present (currently the end of 2024) as a 200-member ensemble. Uncertainty estimates that account for the need to infill for missing observations are made using a Multivariate Gaussian Process, and these are consistent with estimates derived from masking climate model simulations. The use of anisotropic and heterogeneous kernels leads to a reconstruction of El Niño variability whose spatial pattern and temporal variance are generally consistent throughout the record. As compared with taking the unfilled average, infilling increases the global mean surface temperature (GMST) warming estimate over 2005–2024 relative to a 1850–1900 baseline from 1.09 [0.96, 1.18] (95% range across members) to 1.17 [1.05, 1.26]°C, largely because of infilling in rapidly warming high-latitude regions. Compared with HadCRUT5, GISTEMP v4, NOAA Global Temp v6, and Berkeley Earth, DCENT-I shows a steadier and slightly faster GMST warming trend, reflecting the bias-adjustments inherited from DCENT.

1 | Introduction

Century-scale surface-temperature records remain a primary source of evidence for monitoring climate change. The Dynamically Consistent ENsemble of Temperature (DCENT) dataset is a 200-member, monthly 5°×5° surface temperature ensemble spanning 1850–present (currently to the end of 2024) that incorporates recent advances in bias-adjustment (Chan, Gebbie, Huybers, and Kent 2024). These adjustments include (i) breakpoints in station air temperature records (Chan, Gebbie, and Huybers 2024); (ii) group-specific offsets in sea surface temperature (SST) measurements (Chan and Huybers 2019), including the cold truncation bias in early Japanese data that created spurious inter-basin trend contrasts (Chan et al. 2019); (iii) the World War II warm bias (Chan and Huybers 2021); and (iv) early-20th-century cold SST biases that produced land–ocean inconsistencies (Sippel et al. 2024; Chan et al. 2025). Together, these adjustments bring DCENT into closer agreement with independent proxy-based temperatures from tree rings (Chan, Gebbie, Huybers, and Kent 2024) and corals (Chan et al. 2025), and with warming expected from historical radiative forcing (Chan et al. 2025).

Despite its improved bias-adjustments, DCENT provides values only in 5° monthly grid cells where direct observations exist and its coverages diminishes from sampling ~85% of Earth's surface in recent decades to ~25% by the mid-nineteenth century (Chan, Gebbie, Huybers, and Kent 2024). In the 1860s

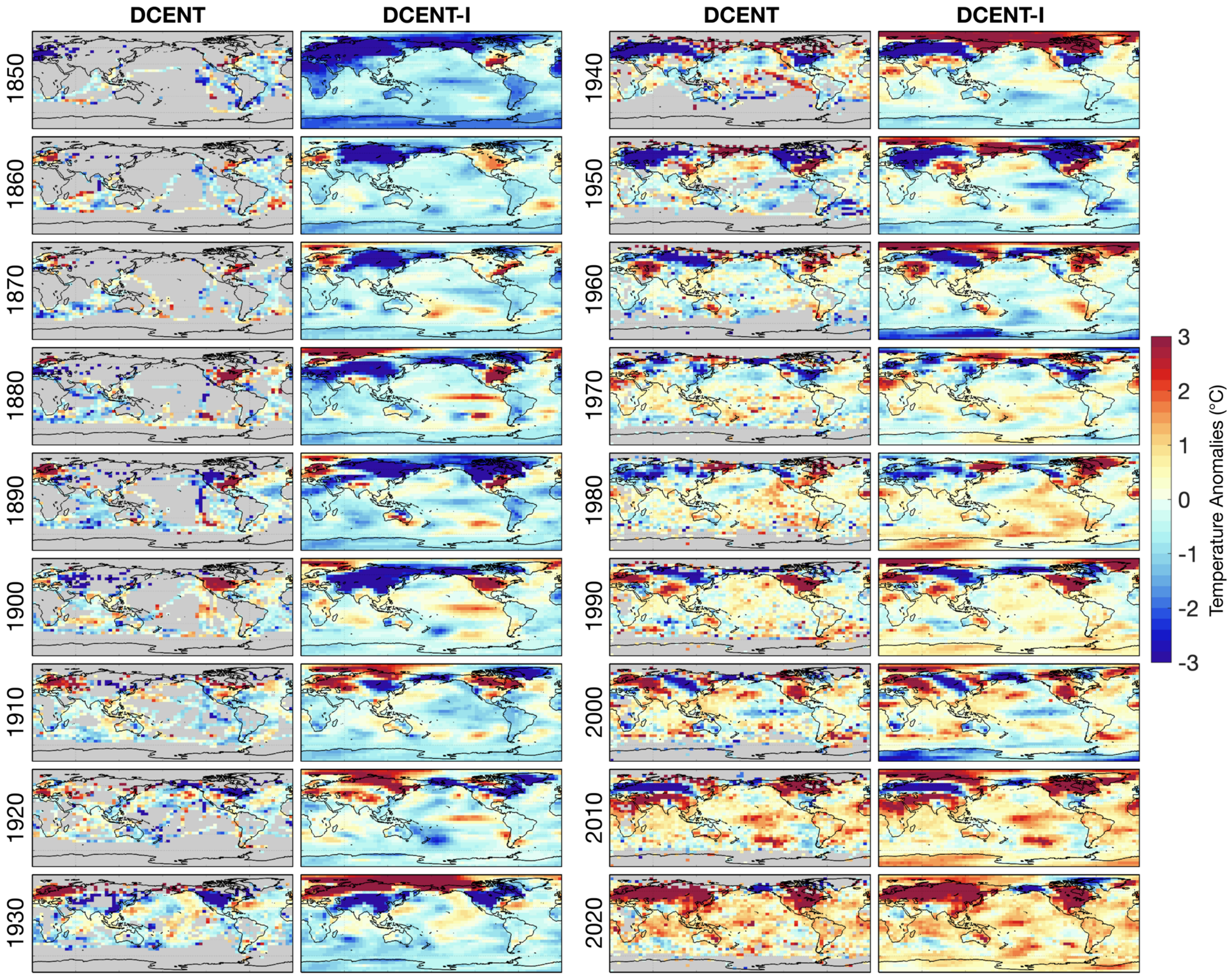

FIGURE 1 | Spatial coverage of temperature anomalies in DCENT and DCENT-I. Surface temperature anomalies (°C) for DCENT (columns 1 and 3) and the infilled DCENT-I (columns 2 and 4) shown for January of the first year in each decade from 1850 to 2020. Anomalies are relative to a 1961–1990 climatology. DCENT values are restricted to grid cells with observational data, while DCENT-I provides spatially complete anomalies.

the only ocean regions observed were the Atlantic, eastern Pacific, and southern Indian Ocean, while land data were confined to Europe and eastern North America (Figure 1). This sparse coverage limits DCENT's utility for studies of, for example, polar amplification (Cowtan and Way 2014) and fails to meet the IPCC AR6 requirement for 'sufficient spatial coverage so that no major regions are systematically excluded' (Gulev et al. 2021).

To satisfy this requirement, we introduce **DCENT-I**, the first spatially infilled ensemble that blends DCENT's state-of-the-art bias corrections with spatially adaptive, anisotropic kriging, to produce globally complete monthly temperature fields with estimates of uncertainty. Here, we distinguish coverage bias, arising from entirely unsampled grid cells, from sampling uncertainty, which reflects errors within partially sampled grid cells. Section 2 overviews the dataset construction. Section 3 discusses the uncertainty due to coverage bias, and Section 4 benchmarks DCENT-I against HadCRUT5 (Morice et al. 2021), NOAA Global Temp v6 (Zhang et al. 2020), GISTEMP v4 (Lenssen et al. 2024), Berkeley Earth (Rohde and Hausfather 2020), and the DCENT-MLE variant following the infilling method in Calvert (2024a). Conclusions are drawn in Section 5 before Section 6 describes access to the data and provides a brief practical usage guide.

2 | DCENT-I Development

The development of DCENT-I begins with the uncombined land surface air temperature (LSAT) and sea surface temperature (SST) anomaly values from the DCENT ensemble. For each of the 200 ensemble members and independently at each time step, LSAT and SST anomalies are spatially interpolated separately using the GloMarGridding software package (Cornes et al. 2025), employing an *Ordinary Kriging* approach. In this framework, the vector of monthly temperature anomalies ($\mathbf{T}'$) is modelled as a multivariate Gaussian distribution, $\mathbf{T}' \sim \mathcal{N}(\mu\mathbb{1}, \Sigma)$, where μ is an a priori unknown global mean, $\mathbb{1}$ is a vector of ones and Σ is the spatial covariance matrix.

The interpolated anomaly field, denoted as $\mathbf{T}'_*$, is thus conditional on the observed anomalies $\mathbf{T}'_\mathbf{o}$ at known locations, and its conditional expectation, denoted by $\mathbb{E}$, is modelled as (Cornes et al. 2025):

$$\mathbb{E}\left(\begin{bmatrix}\mathbf{T}'_* \\ \mu\end{bmatrix} \mid \mathbf{T}'_\mathbf{o}\right) = \begin{bmatrix}\Sigma_{o*}^{\mathrm{T}} \\ \intx^{\mathrm{T}}\end{bmatrix}\begin{bmatrix}\Sigma_{oo} + \mathbf{E} & \intx \\ \intx^{\mathrm{T}} & 0\end{bmatrix}^{-1}\begin{bmatrix}\mathbf{T}'_\mathbf{o} \\ 0\end{bmatrix},$$

where $\mathbf{E}$ is the error covariance matrix, and Σ_{o*} is the spatial covariance matrix between observed and unobserved locations, obtained from subsampling Σ. Similarly, Σ_{oo} is a subsample of Σ at observed locations. Under this approach, the global mean μ is estimated as part of the model fitting. Explicitly accounting for μ avoids damping estimates over sparsely sampled regions towards zero, hence alleviating the potential bias in the global mean associated with underestimating the long-term warming trend. Note that μ is estimated separately for land and ocean domains, allowing the long-term mean change to differ appropriately between air and water temperatures. Our treatment of μ is similar to that used in HadCRUT5 (Morice et al. 2021), but differs from Calvert (2024a), where μ scales a spatial pattern designed to explicitly capture features such as enhanced Arctic warming.

For SST, the error covariance matrix ($\mathbf{E}$) quantifies uncertainty associated with under-sampling of grid-cell values, as well as random measurement errors that are either uncorrelated within a grid-cell, or correlated across grid-cells according to platform ID (such as a travelling ship). These uncertainty values are provided as part of DCENT and are estimated following Kennedy et al. (2011). For LSAT, $\mathbf{E}$ is a diagonal matrix, with uncertainty values estimated as $\sigma^2 = \sigma_0^2 / N$, where N is the number of stations in a grid cell and σ_0^2 is an uncertainty that varies according to month of the year, following Morice et al. (2021).

The spatial covariance matrix (Σ) is developed from anisotropic and heterogeneous elliptic kernels. Parameters of the kernel, that is, local variance, decorrelation lengths of the major and minor axes, and orientation, are estimated empirically using ESA CCI-SST data (Embury et al. 2024) for the marine domain and 2 m air temperature from the ERA5 reanalysis (Hersbach et al. 2020) for terrestrial and sea-ice regions. All grid-cells that have an ESA SST value will receive ellipse parameters representative of the marine domain. For the land domain, if the land-area fraction in a cell is above 0.01 then ellipse parameters will be calculated from ERA5. In addition, any other grid-cell without a value from ESA SST will also receive parameters from ERA5. Details of parameter estimation are provided in section 2.3.2 of Cornes et al. (2025).

Local kernels are stitched together by averaging kernels between point pairs to construct Σ globally for both LSAT and SST (see section 2.3 in Cornes et al. 2025). For completeness, each Σ is extended globally by inserting the global mean of cell-level variance to the diagonal, with off-diagonal elements filled with zero. This ensures that SST observations from the Great Lakes and Caspian Sea, where kernel parameters cannot be estimated because the satellite product lacks lake coverage (Embury et al. 2024), are included in our analysis but assigned limited spatial influence. Temperature estimates are then produced at all grid cells for both LSAT and SST. Having pseudo SST estimates over land in this intermediate step does not affect the final product, since land-only cells have no weight for SST when combining LSAT and SST, and vice versa.

Uncertainty in the interpolated fields is estimated by drawing simulated fields from the Gaussian process posterior distribution for each ensemble member of the input data (see section 2.5 in Cornes et al. 2025). This approach follows Morice et al. (2021) and accounts for both spatial interpolation uncertainty (including in unsampled grid cells) and DCENT's bias-adjustment uncertainty. The posterior covariance used to generate the perturbations is obtained by conditioning the prior covariance model—calibrated using ESA CCI SST (for SST) and ERA5 (for LSAT)—on the available observations. In regions with high data density, the posterior variance is strongly reduced by the data, whereas in sparsely observed or unobserved regions it reverts towards the prior, so the ensemble spread there is governed mainly by the presumed variability rather than local measurements. In addition to quantifying uncertainty, the procedure restores statistically plausible variability to individual ensemble members; variability that is otherwise damped by the interpolation process, especially in data-sparse regions.

In these simulations, each calendar month in each ensemble member has its own random seed, so sampling uncertainty is uncorrelated across months when calculating annual averages. By contrast, Morice et al. (2021) assume full within-year correlation by using a fixed seed across all months. Such an approach is not applicable in our current method because covariance matrices are defined per climatological month. In regions with sparse data, where perturbation uncertainty dominates, our assumption gives annual-mean uncertainties that are smaller by up to a factor of $\sqrt{12}$ compared to Morice et al. (2021). The most appropriate treatment of temporal correlation remains an open question and will be examined in future releases. Another implication of our temporal structure is that, in sparsely sampled regions dominated by perturbation uncertainty, the additional variability introduced by the perturbations is uncorrelated in time, so these under-constrained regions do not gain extra multidecadal variability beyond that represented in μ. Moreover, since LSAT and SST are perturbed independently before being combined, discontinuities may be introduced in individual ensemble members—for example, at the boundary between the Southern Ocean and Antarctica, where sparse observations can lead to large residual errors. Future developments could address this boundary issue by jointly infilling air and sea temperatures, thereby improving spatial continuity in transitional regions.

In the final step, LSAT and SST fields are blended using land fraction in each 5° × 5° grid cell. This is made up of two components: (1) a time invariant mask (A); and (2) a sea-ice fraction mask that varies per month ($\mathrm{sif}(t)$). For the time-invariant mask, the land-area fraction within each 5° cell is computed using the ESA-CCI SST 0.05° land mask (Embury et al. 2024; Lamarche et al. 2017). When calculating land area, each 0.05° subcell is weighted by the cosine of its latitude to account for differences in grid-cell area. In addition, the Caspian Sea and Great Lakes are counted as sea using the definition from MacCallum and Merchant (2011). The monthly varying sea-ice mask is derived from from HadISST2 (Titchner and Rayner 2014) as regions

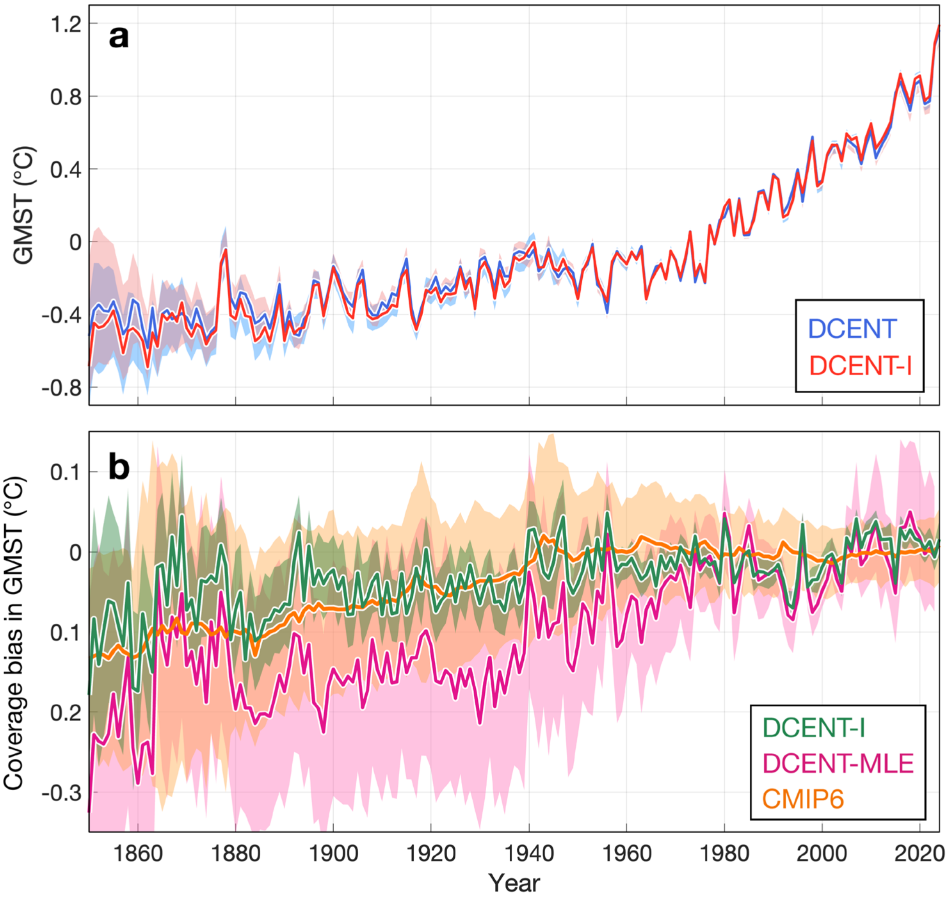

FIGURE 2 | Coverage bias in global mean surface temperature (GMST). (a) GMST anomalies from DCENT (blue) and infilled DCENT-I (red), relative to the 1961–1990 climatology. Shading indicates the 95% confidence interval. (b) Coverage bias in GMST, estimated as DCENT-I minus DCENT (green). Two additional estimates of coverage bias are shown: A maximum-likelihood approach (DCENT-MLE minus DCENT; pink; Calvert 2024a) and a sub-sampling method applied to CMIP6 simulations (orange; Chan et al. 2025). For CMIP6, bias is defined as the difference between GMST from subsampled fields at observed locations and from the full fields. Shading indicates the 95% confidence interval: Across ensemble members for DCENT-I (green shading) and DCENT-MLE (pink shading), reflecting kriging residual error, and across simulations for CMIP6 (orange shading), reflecting internal variability on top of inter-model uncertainty in the forced signal.

with concentrations $>15\%$ on a 1° grid. These two masks are combined as: $\text{Land Weight}(t) = A + (1 - A)\text{sif}(t)$.

3 | DCENT-I Coverage Uncertainty

Figure 1 compares the ensemble mean of DCENT (before infilling) and DCENT-I (after infilling) for the first January of each decade since 1850. Infilling substantially improves coverage in the Arctic and Antarctic throughout the entire historical period, providing a statistically plausible depiction of polar temperatures absent in the original DCENT fields. Greater infilling is required progressively further back in time. During the data-sparse late nineteenth and early twentieth centuries, DCENT-I shows coherent patterns over poorly sampled regions including the Pacific, central Africa, mid- and east Asia, and South America, but we currently lack independent data to evaluate their validity.

Kriging has two features that are useful to highlight. First, kriging tends to damp high-frequency variability and noise and give smoother spatial fields, particularly near the edges of observational coverage, such as the Southern Ocean in the early twentieth century (Figure 1). Second, and more particular to the implementation of Cornes et al. (2025), kriging accounts for partially correlated ship-specific systematic uncertainties, as provided by DCENT, which mitigates the influence of spurious extremes along ship tracks. For example, the unrealistically cold path in January 1890 over the eastern Pacific is reduced in DCENT-I (Figure 1).

On global-mean scales, DCENT-I GMST (red curve in Figure 2a) closely follows the three-stage warming pattern of DCENT GMST computed only over sampled regions (blue curve): a warming trend from 1850–1940, a mid-century hiatus from 1940–1970, and more rapid warming thereafter. The difference between the two (green curve in Figure 2b) represents the coverage bias in DCENT arising from incomplete spatial sampling. This difference is near zero after the 1940s but becomes increasingly negative backward in time, reaching about −0.1°C in the 1850s.

This pattern reflects a baseline-referencing effect: high-latitude regions warm faster than the global mean, so when anomalies are referenced to 1961–1990, early-period high-latitude anomalies are colder than those at lower latitudes. Because the Arctic,

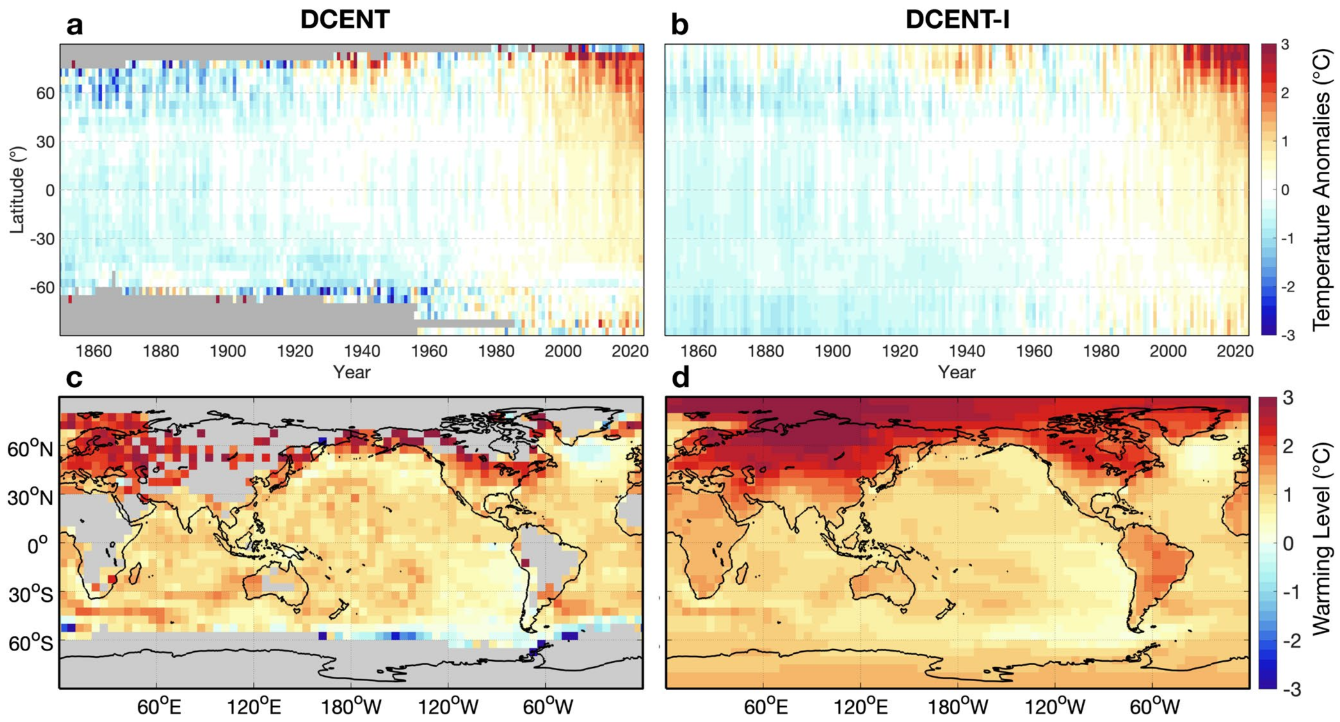

FIGURE 3 | Zonal temperature anomalies and spatial pattern of warming. (a) Zonal mean temperature anomalies from DCENT, relative to the 1961–1990 climatology. (b) As in (a), but for the spatially complete DCENT-I. (c) DCENT warming levels, defined as the 2005–2020 mean temperature anomalies relative to the 1850–1900 baseline. A grid cell is shown if at least one month during the baseline period contains data. (d) As in (c), but for DCENT-I.

Siberia, and northern Canada are sparsely sampled before the mid-twentieth century, their omission causes the non-infilled DCENT fields to overestimate early-period global means relative to DCENT-I. In contrast, although rapid Arctic warming remains incompletely sampled, coverage over high-latitude continents has improved substantially (Figure 1). As a result, the impact of high-latitude under-sampling on the global mean trend has been smaller in recent decades, partly because the Arctic occupies a relatively small area.

For context, Chan et al. (2025) estimated global coverage bias using a CMIP6 subsampling approach (orange curve in Figure 2b). The CMIP6 and DCENT-I estimates are consistent with one another, but the uncertainty due to the coverage bias in DCENT-I, estimated using the ensemble spread, is narrower than that associated with the CMIP6 estimate. This narrower uncertainty estimate arises because the DCENT-I kriging approach is conditioned on observations, thus partially constraining specific contributions of temperature variability. CMIP6 subsampling, in contrast, reflects the full distribution of variability across model simulations.

We also compare our coverage bias estimate with DCENT-MLE (Calvert 2024b; magenta curve in Figure 2b), which is another spatially infilled version of DCENT developed following the method of Calvert (2024a). DCENT-MLE estimates of coverage bias are more negative than those for either DCENT-I or the CMIP6 estimates prior to 1970. This difference appears to stem primarily from the cooler Southern Ocean in DCENT-MLE and, to a lesser extent, cooler Arctic temperatures in the early record, likely related to how sea-ice regions are treated in the DCENT-MLE infilling scheme, discussed further in Section 4.

For zonal-mean temperatures (Figure 3a,b), DCENT-I gives smoother and more complete estimates across all latitudes. The largest changes occur in the Arctic and Southern Ocean prior to 1950, where DCENT-I gives warmer anomalies (also see Figure 1). Additionally DCENT-I provides estimates in latitudinal bands that were unsampled in early DCENT, such as poleward of 75° N and across the Antarctic before the 1960s.

Similar improvements in coverage are evident at the grid-cell level (Figure 3c,d), where DCENT-I infills unobserved regions, including polar oceans, central Africa, and South America. In the Southern Ocean and Antarctic region, the long-term warming pattern is primarily informed by the global mean factor μ and the land–ocean separation rather than by local observations; the stronger warming over Antarctica relative to the surrounding ocean therefore reflects the imposed contrast between land and sea warming rates. Contingent on the assumptions in our kriging approach, DCENT-I also reduces uncertainty in poorly observed marginal regions and yields more spatially coherent patterns. Over relatively well-sampled regions, the overall warming pattern remains similar but becomes smoother, except in the subpolar North Atlantic, where an apparent long-term cooling signal in DCENT is damped in DCENT-I (Figure 3c,d); we return to this difference and its implications in Section 4.

4 | Comparison With Other Estimates

We next compare DCENT-I with other widely used global temperature datasets, including HadCRUT5 (Morice et al. 2021), NOAA Global Temp v6 (Zhang et al. 2020), GISTEMP v4 (Lenssen et al. 2024), Berkeley Earth (Rohde

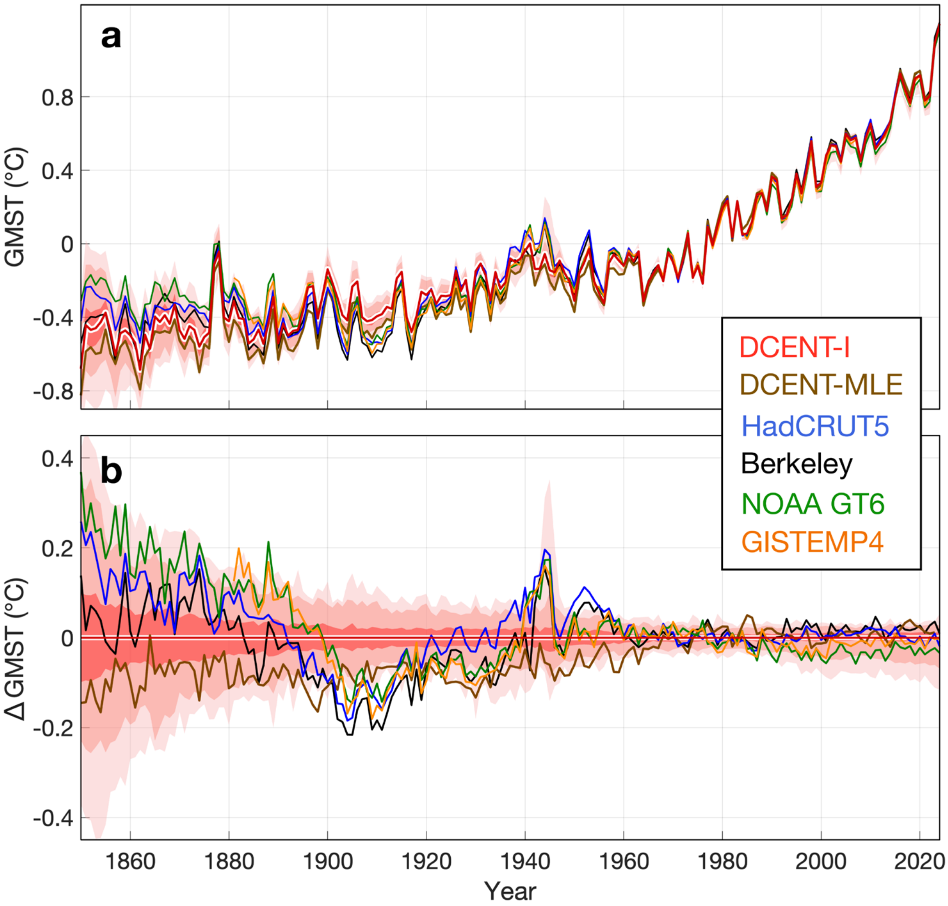

FIGURE 4 | Comparison of GMST estimates. (a) Annual GMST anomalies from DCENT-I (red), DCENT-MLE (brown), HadCRUT5 (blue), Berkeley Earth (black), NOAA GlobalTemp v6 (green), and GISTEMP v4 (orange), relative to the 1961–1990 climatology. For DCENT-I, shading indicates (from light to dark) the ensemble spread, 95% confidence interval, and interquartile range. (b) As in (a), but showing differences relative to the DCENT-I ensemble mean. Note that the DCENT-I ensemble inherits its asymmetry from the underlying DCENT ensemble, which arises from the land homogenisation stage where the parameter-perturbation approach does not impose a Gaussian structure. This produces a skewed distribution, so the percentile envelope is not centred on the mean.

and Hausfather 2020), and the DCENT-MLE variant (Calvert 2024a). The comparison is organised into three parts. Section 4.1 examines global mean surface temperature (GMST), zonal-mean temperatures, and warming levels. Section 4.2 focuses on polar amplification, highlighting the sparsely sampled Arctic region, a key area for characterising anthropogenic warming (Polyakov et al. 2002). Section 4.3 evaluates the representation of El Niño, the dominant mode of interannual climate variability, using tropical Pacific SSTs and the Niño3.4 index.

4.1 | Mean Surface Temperatures

At the global scale, GMSTs from all estimates are consistent with the DCENT-I ensemble after 1960 (Figure 4b). However, notable differences emerge in the late nineteenth and early twentieth centuries. Compared with other estimates not based on DCENT, DCENT-I is cooler during the late 19th century, warmer over 1900–1920, and cooler again during the World War II (Figure 4b).

These differences arise primarily from bias-adjustments applied to raw temperatures, particularly early sea-surface temperature (SST) measurements, rather than from the infilling method itself. Similar differences are, therefore, evident when comparing DCENT with other datasets masked to their common coverage (see figure 8 in Chan, Gebbie, Huybers, and Kent 2024). Chan et al. (2025) analysed the amplitude of the SST diurnal cycle and identified an early transition from wooden to canvas buckets by 1910, accounting for which reduces late 19th century cooling trend (Chan, Gebbie, Huybers, and Kent 2024) and the 1900–1920 cold bias that persists in other estimates (Sippel et al. 2024). The World War II warm anomaly likewise stems from unusual wartime measurement practices already established from the literature, including changes in SST collection methods (Thompson et al. 2008; Chan and Huybers 2021; Kent and Kennedy 2021).

Zonal-mean differences among the datasets (Figure 5) largely mirror the GMST differences discussed above. The late 19th century cooling, early 19th century cold bias, and World War II warm anomaly are evident in the comparison datasets across all frequently sampled latitudes between 60° S and 60° N (Figure 5, right column), indicating that these features are global rather than confined to a single region.

In the Southern Ocean, however, DCENT-MLE is markedly cooler than DCENT-I, with differences exceeding 1°C before 1970

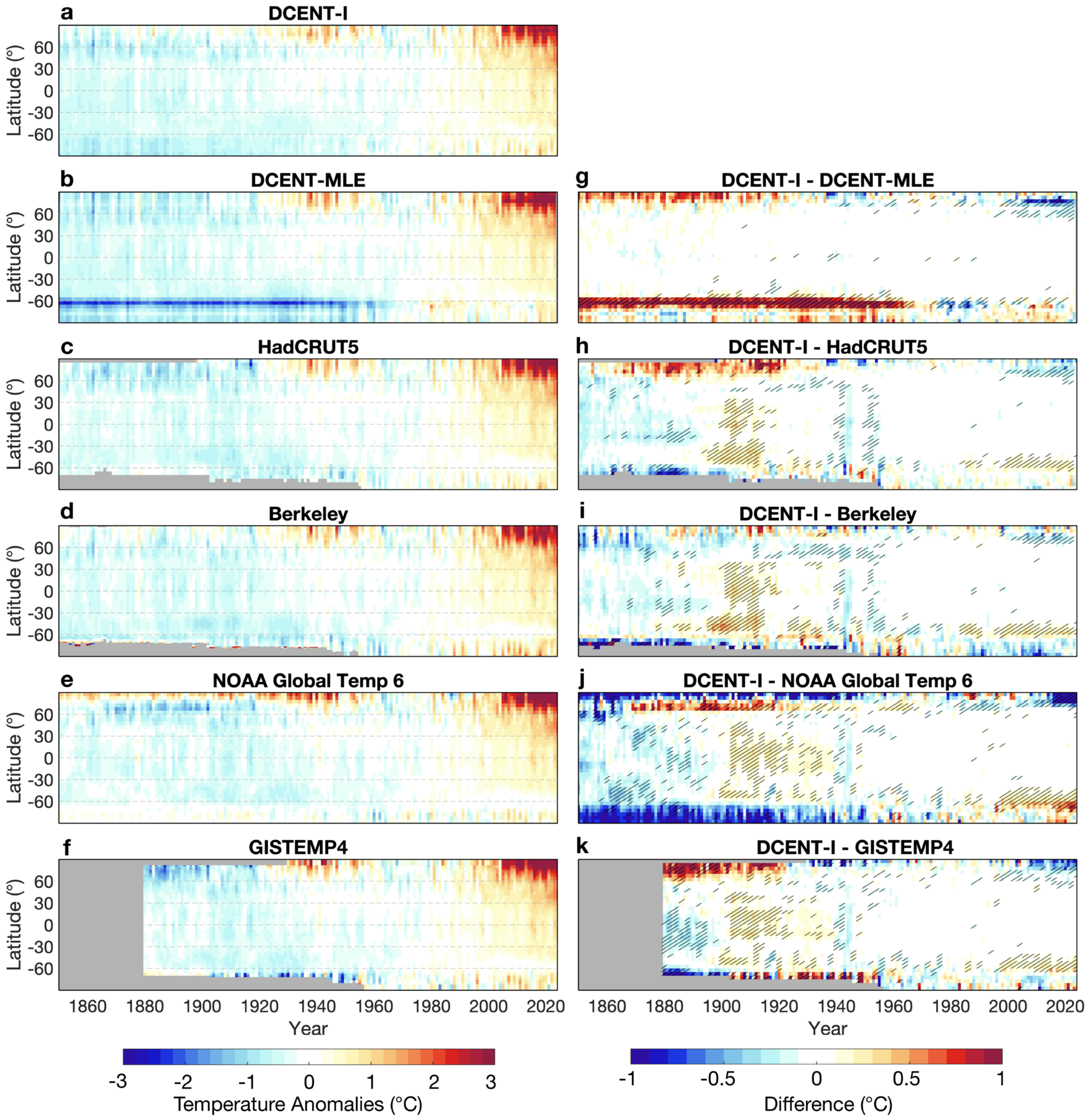

FIGURE 5 | Zonal temperature comparison across datasets. (a) Zonal mean temperature anomalies from DCENT-I, relative to the 1961–1990 climatology. (b–f) As in (a), but for DCENT-MLE, HadCRUT5, Berkeley Earth, NOAA GlobalTemp v6, and GISTEMP v4, respectively. (g) Difference with DCENT-I (DCENT-I minus DCENT-MLE). Shading highlights differences exceeding ±0.1°C that also fall outside the DCENT-I ensemble range. (h–k) As in (g), but for HadCRUT5, Berkeley Earth, NOAA GlobalTemp v6, and GISTEMP v4, respectively.

(Figure 5). A similar cold feature is also seen in the infilled version of HadCRUT5 using the same method (Calvert 2024a, figure not shown). The behaviour in DCENT-MLE arises primarily from the pre-satellite HadISST2 sea-ice fields used to define sea-ice versus open-ocean conditions: HadISST2 shows an apparent loss of roughly 4 million km^2 of Antarctic sea ice prior to the satellite era, a change that appears to be an artefact of how the 1929–1939 German sea-ice climatology is used to construct pre-1979 Southern Ocean fields (Cooper et al. 2025; Dalaiden et al. 2025). Because the DCENT-MLE method incorporates the climatological temperature contrast between ice-covered and open-ocean surfaces into the inferred warming signal (Calvert 2024a), this unrealistic early-century sea-ice retreat hence leads to an exaggerated warming. In contrast, DCENT-I does not rely on this climatological adjustment and is therefore not affected by this artefact.

In the Arctic, DCENT-I shows the smallest warming since 1980 among the compared datasets. Its post-2000 warming level relative to the 1960–1990 climatology is lower by more than 0.3°C compared with NOAA, GISTEMP, and DCENT-MLE,

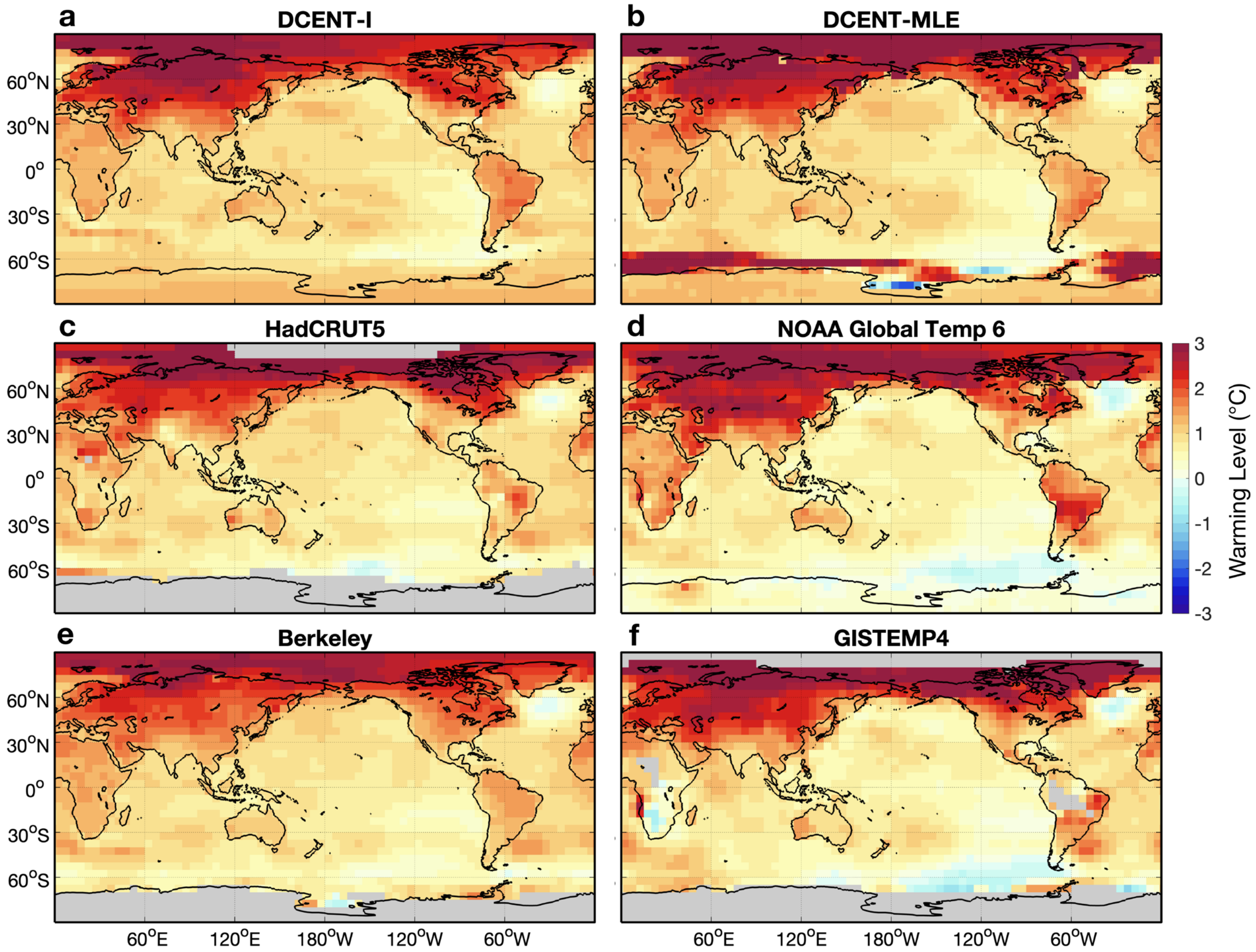

FIGURE 6 | Comparison of warming pattern across datasets. Panels show mean temperature anomalies over 2005–2020 relative to the 1850–1900 baseline, following the format of Figure 3d. Results are shown for (a) DCENT-I, (b) DCENT-MLE, (c) HadCRUT5, (d) NOAA GlobalTemp v6, (e) Berkeley Earth, and (f) GISTEMP v4.

and slightly weaker, by ~0.2°C, but still significant relative to HadCRUT5 and Berkeley Earth. In Section 4.2, we provide a more detailed analysis of the potential cause of this difference.

Figure 6 compares the spatial patterns of surface warming across datasets. All products show broadly similar large-scale features, including amplified warming over land and in the Arctic. DCENT-based products (DCENT-I and DCENT-MLE) are generally more consistent with datasets based on the Met Office Hadley Centre SST (HadSST4, Kennedy et al. 2019), that is, HadCRUT5 and Berkeley Earth, than with datasets based on NOAA's Extended Reconstructed SST (ERSST, Huang et al. 2017), that is, NOAA Global Temp v6 and GISTEMP v4. In particular, in the 180° W–60° W sector of the Southern Ocean, DCENT-based and HadSST-based products show slight warming, whereas ERSST-based products show cooling.

All datasets also capture the North Atlantic 'cold blob,' though its magnitude is weaker in DCENT-based and HadSST-based products than in ERSST-based products. Given that the cold blob is as pronounced in the non-infilled DCENT (Figure 3c) as ERSST-based products, this difference highlights a need for further work to assess how infilling and underlying SST reconstructions affect the representation of this regional feature. Finally, the sharp transition near 60° N in NOAA Global Temp v6, which is absent in other datasets, suggests a possible artefact of the underlying analysis.

Overall, DCENT-I retains the bias-adjustment advances of DCENT and indicates a steadier and slightly larger historical warming. Infilling enables global coverage and yields large-scale warming patterns consistent with other datasets. That said, differences in, for example, the magnitude of Arctic warming and the North Atlantic Cold Blob still call for the need of further investigation into the influence of infilling methods. DCENT-I, therefore, offers a reliable baseline for historical warming estimates while pointing to specific regions that merit closer scrutiny.

4.2 | Arctic Warming

From the zonal-mean comparison in Section 4.1, we noted that DCENT-I shows slightly cooler temperature anomalies than

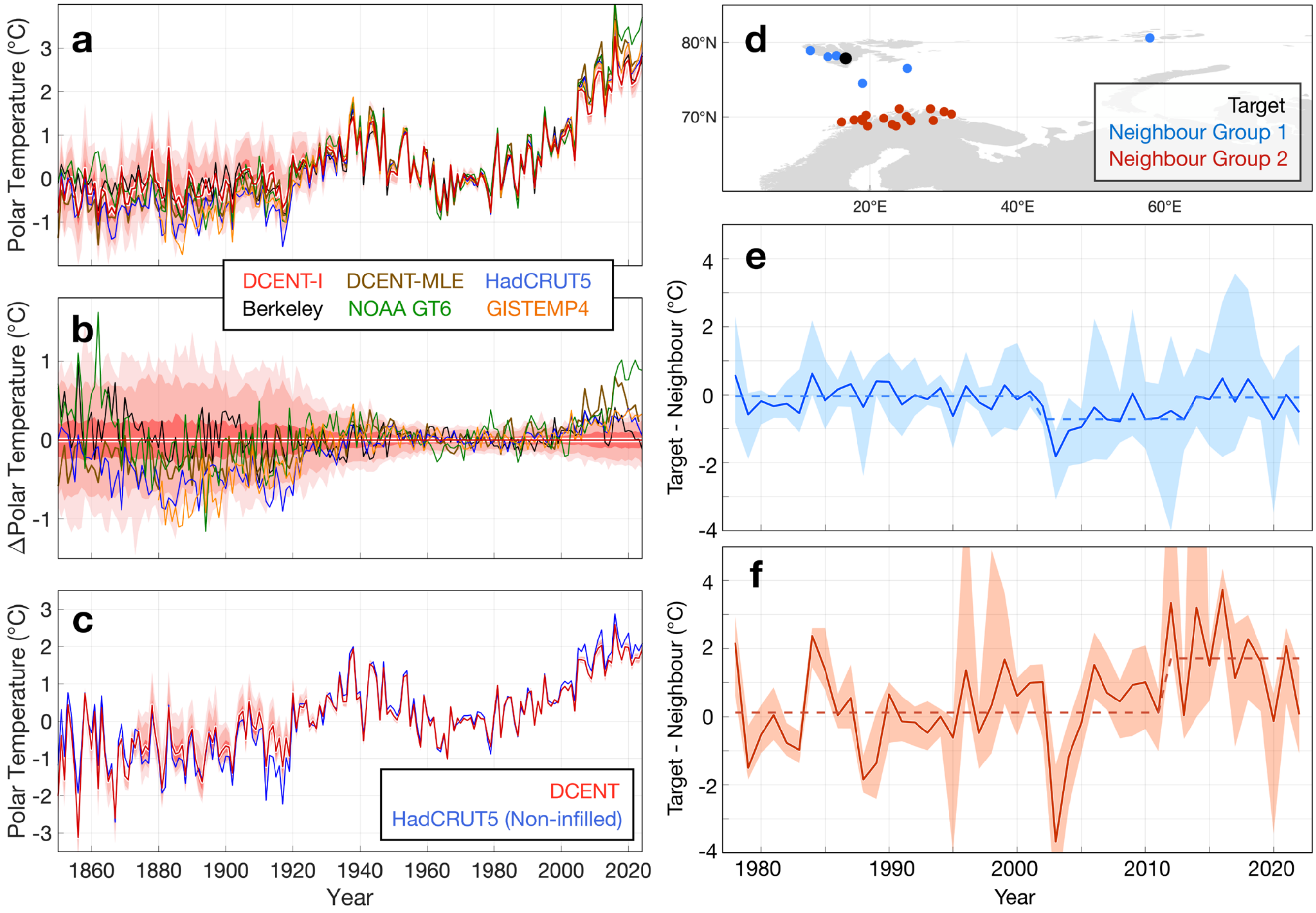

FIGURE 7 | Arctic temperature comparison. (a) As in Figure 4a, but showing temperature anomalies averaged over the Arctic (70° N and poleward). (b) As in (a), but showing differences relative to the DCENT-I ensemble mean. (c) As in (a), but for non-infilled datasets: DCENT (red) and HadCRUT5 (blue). (d, f) An example of pairwise homogenisation for land station temperatures. (d) Locations of stations in a regional network: The target station (black), neighbours poleward of 72° N (Group 1; blue, 7 stations), and neighbours below 72° N (Group 2; red, 19 stations). (e) Mean temperature differences between the target station and neighbours in Group 1. Shading denotes the 95% confidence interval, and dashed lines mark breakpoints detected by the pairwise comparison algorithm of Chan, Gebbie, and Huybers (2024). (f) As in (d), but for Group 2 neighbours.

other datasets since the 2000s. Because polar amplification is of particular scientific interest, we now examine potential causes of this difference by focusing on Arctic temperatures (70° N poleward; Figure 7a).

When conditioned on the 1960–1990 mean, DCENT-I shows the lowest Arctic temperature anomalies (ATA) over 2000–2024 among all estimates (Figure 7b), being, on average, 0.15°C cooler than Berkeley Earth, 0.21°C cooler than HadCRUT5, 0.22°C cooler than GISTEMP, 0.35°C cooler than DCENT-MLE, and 0.44°C cooler than NOAA Global Temp v6.

Such a difference could arise from differences in the non-infilled data, the infilling method, or both. Comparing the non-infilled ensembles (Figure 7c) shows that DCENT is about 0.24°C cooler than HadCRUT5, pointing to raw data and bias-adjustments as the main source of the difference between HadCRUT5 and DCENT-I.

One likely contributor is the pairwise homogenisation algorithm applied in DCENT (Chan, Gebbie, and Huybers 2024). This method compares each station against its neighbours and adjusts detected breakpoints accordingly. An example from Svalbard is shown in Figures 7d–f, where a target station (black circle) is compared against two neighbour groups: a polar group poleward of 72° N and otherwise a continental group (Figures 7d). For the polar group, the algorithm detects two breakpoints with offsetting effects, yielding no net trend change (Figure 7e). For the continental group, however, a significant upward jump of more than 1.5°C in 2012 is detected (Figure 7f). Because the adjustment is estimated using all neighbours, the larger number of continental stations dominates, leading to a downward adjustment of the target polar station and presumably its close neighbours when they are considered. Similar sensitivities of large-scale homogenisation algorithms to heterogeneous regional trends and reference series have also been documented in other datasets such as for northern Canada in the Berkeley Earth temperature product (Way et al. 2017).

While this outcome is consistent with the algorithm's design, the coherence among polar stations raises the question of whether such cooling adjustments are fully justified. This points to a potential need for improved homogenisation approaches that weight neighbours by distance or apply a multivariate Gaussian process to account more explicitly for spatial and temporal covariance.

The remaining differences between DCENT-I and DCENT-MLE must arise from the infilling step, as both datasets use the same input data. DCENT-MLE applies an explicit latitudinal amplification function, which increases warming towards the pole, potentially leading to warmer Arctic anomalies than in DCENT-I.

Similarly, the 0.58°C difference over 2016–2024 between NOAA Global Temp v6 and GISTEMP, both of which rely on GHCNmV4 (Menne et al. 2018) and ERSST5 (Huang et al. 2017), should reflect differences in infilling. Notably, the post-2016 Arctic warming in NOAA Global Temp v6 appears particularly large and abrupt (Figures 5 and 7), which warrants further scrutiny but is beyond the scope of this paper.

4.3 | El Niño Events

DCENT-I reconstructs historical El Niño events with spatially realistic patterns, even during periods of sparse data coverage. For example, the December 1877 El Niño (Figure 8a) is represented by a coherent equatorial Pacific warming pattern in DCENT-I. HadCRUT5 and Berkeley Earth appear less coherent, presumably because of their use of globally homogeneous and isotropic kernels at a time when data density is diminished. DCENT-MLE reproduces the large-scale El Niño pattern more distinctly because it incorporates the leading EOF of surface temperature into its model specification, but its amplitude is weaker, potentially reflecting regression dilution when a fixed pattern is used to represent event-to-event variability. DCENT-I gives results most comparable to those of NOAA Global Temp v6, whose AI-based method leverages long-range teleconnections. Similar results are seen for the February 1941 El Niño (Figure 8b), showing that DCENT-I represents major El Niño events that are more in keeping with better-sampled modern realisations than those obtained from kriging using homogeneous and isotropic kernels with smaller zonal extent in tropical regions.

ENSO variability, measured by the Niño3.4 index, further supports these findings (Figure 8c,d). Between 1880 and present, DCENT-I shows variability similar to the post-1980 satellite era and to NOAA Global Temp v6, whereas HadCRUT5, Berkeley Earth, and DCENT-MLE exhibit a marked decrease, with running 30-year standard deviations falling to ~70% of those in DCENT-I and NOAA Global Temp v6.

Although all datasets assume stationarity in their covariance structures, the fact that HadCRUT5 and Berkeley Earth produce lower interannual variability is readily understood, because they use a globally uniform decorrelation length that is shorter than the long decorrelation length at the equator. Without direct observations near the Niño3.4 region, the kriged estimates are damped, leading to underestimated ENSO variability. DCENT-I applies a longer decorrelation length in constructing its covariance matrix, thereby reducing this damping effect. That said, whether DCENT-I reliably maps sparse tropical Pacific observations, often limited to a few grid cells (Figure 8a), and avoids overestimating variability remains an open question. Prior to 1880, the ensemble-mean variability in DCENT-I declines (dark red in Figure 8d), reflecting the very sparse sampling of the tropical Pacific during the 1860s and early 1870s. NOAA's AI-based approach shows a similar but smaller drop, likely because it includes teleconnections and, thus, data from greater distance. Whether these teleconnections are stable, however, is unclear (Alizadeh 2024). The agreement with DCENT-I, whose perturbation of ensemble members using residual errors preserves event-scale variance (Figure 8c), is an important check on the overall stability of ENSO variability (red in Figure 8d).

5 | Conclusion

DCENT-I is a spatially complete, ensemble-based global temperature dataset that combines the bias-adjustment advances of DCENT with a open-source kriging-based infilling approach. By comparing DCENT-I against widely used datasets, we demonstrated that it provides consistent global mean surface temperature estimates since the mid-20th century, while resolving key historical differences in the late 19th and early 20th centuries that arise primarily from bias-adjustments rather than infilling. DCENT-I reproduces large-scale temperature patterns, such as faster land and Arctic warming. It also reproduces visually realistic historical El Niño events while maintaining variance similar to the modern period back to at least the late 1880s.

These results highlight DCENT-I as a reliable tool for historical warming assessments and a valuable resource for climate monitoring, model evaluation, and policy-relevant analysis. At the same time, remaining differences, most notably in the magnitude of recent Arctic warming, the North Atlantic 'cold blob,' and the treatment of Southern Ocean sea-ice regions, point to specific areas for further investigation. Addressing these questions will strengthen understanding of regional climate behaviour.

Finally, DCENT-I has a 5° × 5° resolution, matching the underlying DCENT dataset. The coarse 5° resolution is a known limitation for some applications. Moving to finer spatial scales would require a separate high-resolution reconstruction framework and substantially greater computational resources, as well as careful consideration of ensemble size and data volume. These steps are feasible but beyond the scope of the present release. Future releases of DCENT and DCENT-I will explore higher-resolution options as methodological developments and computational capacity allow.

6 | Data Access and Usage Guide

6.1 | Access to DCENT-I

DCENT-I is available via Harvard Dataverse (https://doi.org/10.7910/DVN/ROG38Q) and is under submission at CEDA (https://doi.org/10.5285/4600d26e-b3f1-9a8a-e063-7086abc0fa44). Each member's file is named in the format of 'DCENT_I_1.1.0.0_member_ [XXX].nc,' with the variables described in Table 1. The ensemble mean and spread are also provided in 'DCENT_I_1.1.0.0_mean_spread_ts/lsat/sst.nc,' together with monthly 1982–2014 climatological temperatures in 'DCENT_I_1.1.0.0_clim_1982_2014.nc' to facilitate

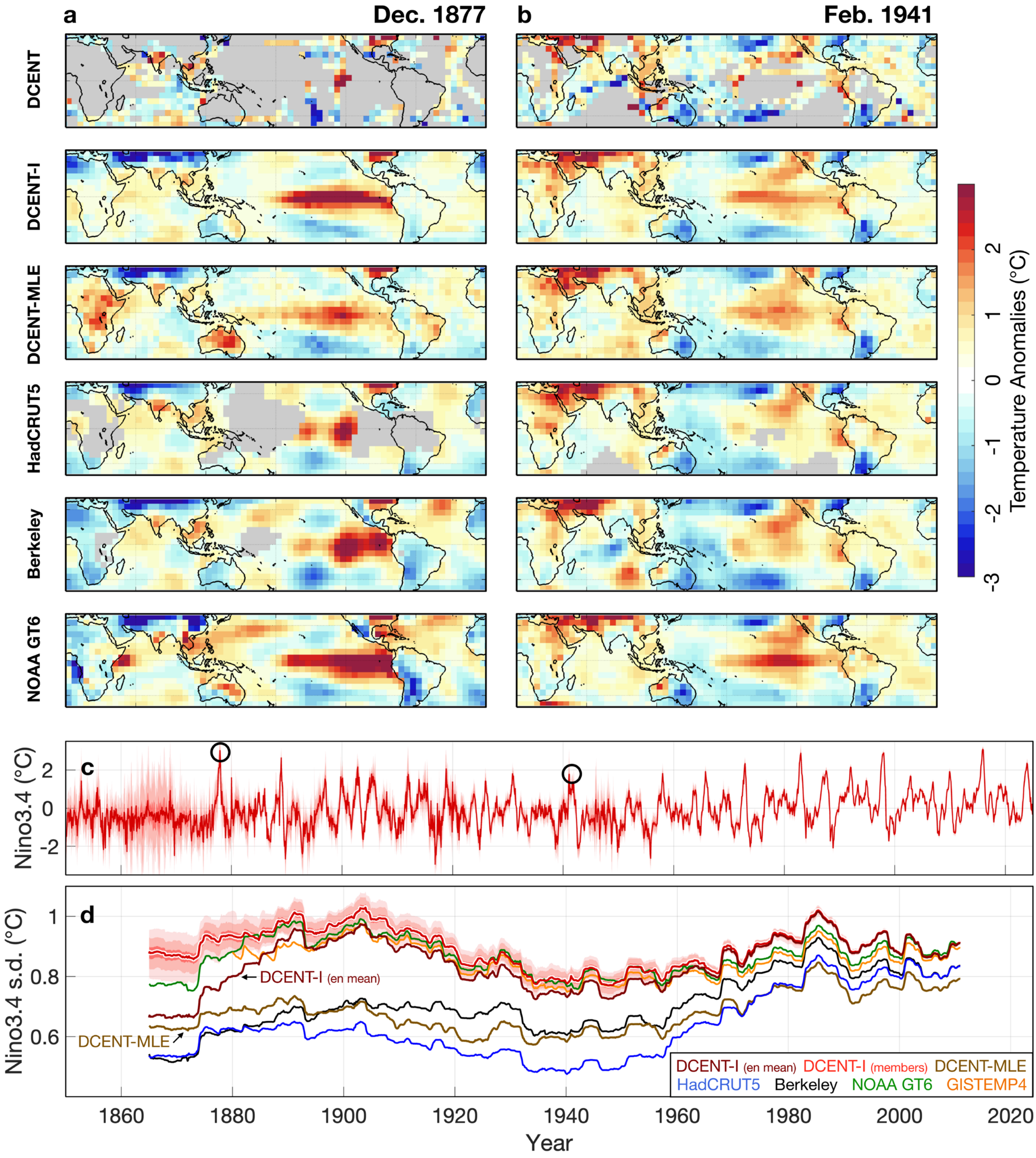

FIGURE 8 | Reconstruction of historical El Niño events and ENSO variability. (a) December 1877 temperature anomalies (°C), relative to the 1960–1990 climatology, from DCENT, DCENT-I, DCENT-MLE, HadCRUT5, Berkeley Earth, and NOAA GlobalTemp v6 (top to bottom). GISTEMP v4 is excluded as its record begins in 1880. All datasets are first regridded to a common 5° resolution. (b) As in (a), but for February 1941. (c) Monthly Niño3.4 index in DCENT-I, defined as the mean SST anomalies over 5° S–5° N, 170° W–120° W. Circles indicate the months plotted in (a) and (b). (d) Sliding standard deviation of the Niño 3.4 index over a 30-year (360-month) window, plotted by centred month, as in Figure 4a.

the determination of absolute temperatures. The climatology file is identical to that for DCENT. A 'DCENT_I_1.1.0.0_diagnostics.nc' file provides land/sea masks and weighting. This file also reports a data reliability indicator, calculated as one minus the fraction of residual kriging variance relative to the prior variance (sst_α and $lsat\_\alpha$), which users may apply to mask low-confidence regions as needed. To support users requiring access through cloud computing, DCENT-I is also available in .zarr format in the Google Cloud bucket 'dcent-i-zarr.' A Jupyter notebook script for accessing DCENT-I on

TABLE 1 | Details of variables in DCENT-I individual members.

Variable	Long name	Description
lon	Longitude	Longitude of 5° cell centre (2.5° E to 357.5° E)
lon_bnds	Longitude bounds	Lower and upper longitude boundaries of each cell
lat	Latitude	Latitude of 5° cell centres (87.5° S to 87.5° N)
lat_bnds	Latitude bounds	Lower and upper latitude bounds of each cell
time	Time	Days since Jan. 1, 1850 (standard calendar)
time_bnds	Time bounds	Start and end of each time step
ts	Surface temperature anomaly	**DCENT-I**: Blended 2 m air temperature anomalies over land and sea ice with sea surface temperature anomalies over open ocean, relative to the 1982–2014 climatology (in °C)
lsat	Land surface air temperature anomaly	**DCLSAT-I**: 2 m air temperature anomalies over land and sea-ice, relative to the 1982–2014 climatology (in °C)
sst	Sea surface temperature anomaly	**DCSST-I**: Sea surface temperature anomalies over open and ice-covered ocean, relative to the 1982–2014 climatology (in °C)
realisation	Realisation	Ensemble member index

Google Cloud is available at https://doi.org/10.7910/DVN/ROG38Q.

In addition to gridded products, global and hemispheric summary statistics of DCENT-I can be downloaded from https://duochanatharvard.github.io/#DCENT.

6.2 | DCENT-I Usage Guide

Similar to DCENT, DCENT-I is suitable for monitoring and quantifying historical and recent trends and variability, detecting and attributing surface temperature changes, validating and constraining climate models, and informing policy goals aimed at mitigating climate change. Because the product retains a 5° × 5° resolution, users should exercise caution in regions where land–ocean contrasts occur within a single grid cell. In such cases, it could be useful to consider the infilled land-only (DCLSAT-I) or ocean-only (DCSST-I) products (see Table 1), especially when comparing with proxies that represent exclusively terrestrial or marine conditions. With spatial infilling, DCENT-I can also be used as a boundary condition for AMIP-type model experiments, provided it is first combined with climatological fields and interpolated to the required model resolution. A sample file with the ensemble mean of the infilled SST fields, interpolated and added to the 1° × 1° 1982–2014 OISST climatology, is available at https://duochanatharvard.github.io/#DCENT. However, because DCENT-I is monthly, and its variability is based on the standard 5° version, neither variant is intended for fully resolving synoptic-scale extreme events, such as marine heat waves.

Each ensemble member from DCENT represents a variation in the bias-adjustments applied which are thought to be equally likely. The DCENT-I ensemble takes each of the DCENT ensemble members and perturbs the field as described in Section 2 and in more detail by Cornes et al. (2025) to represent the combined effect of the measurement uncertainty in the DCENT grid cells and the uncertainty due to coverage bias arising from missing grid cells. It is recommended that either the full ensemble is used in analysis, or for applications where that is not practical, the ensemble mean and spread is used.

Because DCENT-I is spatially complete, it is directly comparable to other spatially complete fields, such as NOAA Global Temperature v6. Other estimates, such as HadSST5 and Berkeley Earth, infill data but mask grid cells far away from sampled cells, resulting in missing values in the late 19th century (e.g., maps in Figure 8). For these products we have used GMST estimates from the data providers, rather than calculating them ourselves from the gridded products, as these account for coverage biases. For regional comparisons, masking data to common coverage across data products before averaging is recommended.

To compare DCENT-I against model output, we recommend using the model's full global coverage without masking. However, because DCENT-I uses SST over the open ocean and air temperature over sea-ice regions, model comparisons should use simulated temperature anomalies from the variable 'tos' for open-ocean grid points and 'tas' for grid cells covered by sea ice.

6.3 | Supporting Data Access

The following data products were used in the construction of DCENT-I described in Section 2.

- The DCENT V2.0 ensemble (Chan, Gebbie, Huybers, and Kent 2024) is available from the Harvard Dataverse: https://doi.org/10.7910/DVN/NU4UGW. Accessed 2025-05-01.
- The sea ice concentration estimates from HadISST2.2.2.0 (Titchner and Rayner 2014) were downloaded from the UK Met Office: https://www.metoffice.gov.uk/hadobs/hadisst2/. Accessed 2025-06-01.

- The satellite data used in the construction of the SST covariance matrix and land ocean mask (Embury et al. 2024) were downloaded from the University of Reading via their regridding service: https://surftemp.net/. Accessed 2024-10-01.
- The ERA5 air temperatures (Hersbach et al. 2020) used in the construction of the covariance matrix over land and sea ice were downloaded from the Centre for Environmental Data Analysis: https://catalogue.ceda.ac.uk/uuid/c1145ccc4b6d4310a4fc7cce61041b63/ (Centre for Environmental Data Analysis 2024) Registration required. Accessed 2024-06-01.

The following data products were used in the evaluation of DCENT-I presented in Section 4.

- DCENT-MLE (Calvert 2024b): https://www.wdc-climate.de/ui/entry?acronym=DCENT_MLE_v1_0. Accessed 2025-05-15.
- HadCRUT5 (Morice et al. 2021): https://www.metoffice.gov.uk/hadobs/hadcrut5/. Accessed 2025-06-24.
- GISTEMP v4 (Lenssen et al. 2019, 2024): https://data.giss.nasa.gov/gistemp/. Accessed 2025-06-25.
- Berkeley Earth (Rohde and Hausfather 2020): https://berkeleyearth.org/data/. Accessed 2025-06-25.
- NOAAGlobalTemp v6 (Yin et al. 2024; Huang et al. 2025a, 2025b): https://www.ncei.noaa.gov/products/land-based-station/noaa-global-temp Huang et al. (2024). Accessed 2025-06-25.

6.4 | Code Availability

Code to reproduce DCENT-I, including estimating kernel parameters, performing Gaussian-process interpolation, and combining land and ocean temperature estimates, is available at https://github.com/NOCSurfaceProcesses/DCENT-infilling.

Acknowledgements

D.C. is supported by a UKRI Future Leaders Fellowship Award (UKRI2360). The contributions of A.F., S.C., J.S., A.C., R.C., and E.K. were funded by UKRI/NERC via the National Oceanography Centre National Capability Program AtlantiS (grant number NE/Y005589/1). G.G. is supported by US NSF OCE-2122805. P.H. is supported by US NSF Award 2123295. We acknowledge the ESA Climate Change Initiative and the SST CCI project for providing the data used in this paper and the Met Office for the HadISST.2.2.0.0 sea ice concentration data. ERA5 data were provided by the Copernicus Climate Change Service (C3S). The authors acknowledge the ECMWF for producing and maintaining the ERA5 dataset. We are grateful for discussions with Dr. Colin Morice at the Met Office on the implementation of the HadCRUT5 gridding methodology, which has guided some aspects of the approach taken in this paper.

Funding

This work was supported by a UKRI Future Leaders Fellowship Award (UKRI2360), the UK National Oceanography Centre National Capability Program AtlantiS (grant number NE/Y005589/1), and US NSF Awards OCE-2122805 and 2123295.

Disclosure

Dataset Details: DCENT-I is a globally complete, 200-member ensemble of monthly surface temperature anomalies at 5°×5° resolution, spanning the period from 1850 to present. It is derived from the unfilled DCENT dataset and represents 2-m air temperature anomalies over land and sea ice and sea surface temperature (SST) anomalies over the open ocean. In addition to the ensemble realisations, summary statistics—including the ensemble mean, standard deviation, and the 5th and 95th percentiles—are provided. All temperature values are expressed as anomalies relative to the 1982–2014 climatology, which is also supplied to enable reconstruction of monthly absolute temperatures. A diagnostics file is provided, which contains the land/sea weights and masks, as well as a data reliability indicator (α), which represents one minus the proportion of the residual kriging variance relative to the prior variance.

Identifier: https://doi.org/10.7910/DVN/ROG38Q

Creator: University of Southampton, National Oceanography Centre, Woods Hole Oceanographic Institution, and Harvard University.

Dataset correspondence: duo.chan@soton.ac.uk

Title: DCENT-I: an infilled version of DCENT.

Publisher: Harvard Dataverse (https://doi.org/10.7910/DVN/ROG38Q) and under submission to CEDA (https://doi.org/10.5285/4600d26e-b3f1-9a8a-e063-7086abc0fa44).

Publication year: 2026.

Resource type: Dataset.

Version: 1.1.0.0.

Conflicts of Interest

The authors declare no conflicts of interest.

Data Availability Statement

The data that support the findings of this study are openly available in Harvard Dataverse at https://doi.org/10.7910/DVN/ROG38Q.

References

Alizadeh, O. 2024. "A Review of ENSO Teleconnections at Present and Under Future Global Warming." *WIREs Climate Change* 15, no. 1: e861.

Calvert, B. T. 2024a. "Improving Global Temperature Datasets to Better Account for Non-Uniform Warming." *Quarterly Journal of the Royal Meteorological Society* 150, no. 763: 3672–3702.

Calvert, B. T. T. 2024b. "Maximum Likelihood Estimates of Temperatures Using Data From the Dynamically Consistent Ensemble of Temperature (Version 1.0)." https://www.wdc-climate.de/ui/entry?acronym=DCENT_MLE_v1_0.

Centre for Environmental Data Analysis. 2024. "European Centre for Medium-Range Weather Forecasts (2021): ECMWF ERA5: Surface Level Analysis Parameter Data." Accessed 1 June 2024. https://catalogue.ceda.ac.uk/uuid/c1145ccc4b6d4310a4fc7cce61041b63/.

Chan, D., G. Gebbie, and P. Huybers. 2024. "An Improved Ensemble of Land-Surface Air Temperatures Since 1880 Using Revised Pair-Wise Homogenization Algorithms Accounting for Autocorrelation." *Journal of Climate* 37, no. 7: 2325–2345.

Chan, D., G. Gebbie, and P. Huybers. 2025. "Re-Evaluating Historical Sea Surface Temperature Data Sets: Insights From the Diurnal Cycle, Coral Proxy Data, and Radiative Forcing." *Geophysical Research Letters* 52: e2025GL116615. https://doi.org/10.1029/2025GL116615.

Chan, D., G. Gebbie, P. Huybers, and E. C. Kent. 2024. "A Dynamically Consistent ENsemble of Temperature at the Earth Surface Since 1850 From the DCENT Dataset." *Scientific Data* 11, no. 1: 953.

Chan, D., and P. Huybers. 2019. “Systematic Differences in Bucket Sea Surface Temperature Measurements Among Nations Identified Using a Linear-Mixed-Effect Method.” *Journal of Climate* 32, no. 9: 2569–2589.

Chan, D., and P. Huybers. 2021. “Correcting Observational Biases in Sea Surface Temperature Observations Removes Anomalous Warmth During World War II.” *Journal of Climate* 34, no. 11: 4585–4602.

Chan, D., E. C. Kent, D. I. Berry, and P. Huybers. 2019. “Correcting Datasets Leads to More Homogeneous Early-Twentieth-Century Sea Surface Warming.” *Nature* 571, no. 7765: 393–397.

Cooper, V. T., G. J. Hakim, and K. C. Armour. 2025. “Monthly Sea Surface Temperature, Sea Ice, and Sea Level Pressure Over 1850–2023 From Coupled Data Assimilation.” *Journal of Climate* 38, no. 19: 5461–5490.

Cornes, R. C., S. C. Chan, A. Cable, et al. 2025. “GloMarGridding: A Python Toolkit for Flexible Spatial Interpolation in Climate Applications.” Submitted to *Geoscience Data Journal*, PREPRINT (Version 1) Available At *Research Square*. https://doi.org/10.21203/rs.3.rs-7427869/v1.

Cowtan, K., and R. G. Way. 2014. “Coverage Bias in the HadCRUT4 Temperature Series and Its Impact on Recent Temperature Trends.” *Quarterly Journal of the Royal Meteorological Society* 140, no. 683: 1935–1944.

Dalaiden, Q., H. Goosse, P. R. Holland, and A. Barthelemy. 2025. “Dynamical Reconstruction of Southern Ocean and Antarctic Climate Variability Since 1700.” *Scientific Data* 12, no. 1: 1574.

Embury, O., C. J. Merchant, S. A. Good, et al. 2024. “Satellite-Based Time-Series of Sea-Surface Temperature Since 1980 for Climate Applications.” *Scientific Data* 11, no. 1: 326.

Gulev, S. K., P. W. Thorne, J. Ahn, et al. 2021. “Changing State of the Climate System.” In *Climate Change 2021: The Physical Science Basis. Contribution of Working Group I to the Sixth Assessment Report of the Intergovernmental Panel on Climate Change*. Book Section 2. Cambridge University Press.

Hersbach, H., B. Bell, P. Berrisford, et al. 2020. “The ERA5 Global Reanalysis.” *Quarterly Journal of the Royal Meteorological Society* 146, no. 730: 1999–2049.

Huang, B., P. W. Thorne, V. F. Banzon, et al. 2017. “Extended Reconstructed Sea Surface Temperature, Version 5 (ERSSTv5): Upgrades, Validations, and Intercomparisons.” *Journal of Climate* 30, no. 20: 8179–8205.

Huang, B., X. Yin, T. Boyer, et al. 2025a. “Extended Reconstructed Sea Surface Temperature, Version 6 (ERSSTv6). Part I: An Artificial Neural Network Approach.” *Journal of Climate* 38, no. 4: 1105–1121. https://doi.org/10.1175/JCLI-D-23-0707.1.

Huang, B., X. Yin, T. Boyer, et al. 2025b. “Extended Reconstructed Sea Surface Temperature, Version 6 (ERSSTv6). Part II: Upgrades on Quality Control and Large-Scale Filter.” *Journal of Climate* 38, no. 4: 1123–1136. https://doi.org/10.1175/JCLI-D-24-0185.1.

Huang, B., X. Yin, M. J. Menne, R. S. Vose, and H. M. Zhang. 2024. “NOAA Global Surface Temperature Dataset (NOAAGlobalTemp), Version 6.0.” https://www.ncei.noaa.gov/metadata/geoportal/rest/metadata/item/gov.noaa.ncdc:C01704/html.

Kennedy, J., N. Rayner, C. Atkinson, and R. Killick. 2019. “An Ensemble Data Set of Sea Surface Temperature Change From 1850: The Met Office Hadley Centre HadSST. 4.0.0.0 Data Set.” *Journal of Geophysical Research: Atmospheres* 124, no. 14: 7719–7763.

Kennedy, J., N. Rayner, R. Smith, D. Parker, and M. Saunby. 2011. “Reassessing Biases and Other Uncertainties in Sea Surface Temperature Observations Measured in Situ Since 1850: 1. Measurement and Sampling Uncertainties.” *Journal of Geophysical Research* 116, no. D14104.

Kent, E. C., and J. J. Kennedy. 2021. “Historical Estimates of Surface Marine Temperatures.” *Annual Review of Marine Science* 13: 283–311.

Lamarche, C., M. Santoro, S. Bontemps, et al. 2017. “Compilation and Validation of SAR and Optical Data Products for a Complete and Global Map of Inland/Ocean Water Tailored to the Climate Modeling Community.” *Remote Sensing* 9, no. 1: 36. https://doi.org/10.3390/rs9010036.

Lenssen, N., G. A. Schmidt, M. Hendrickson, P. Jacobs, M. J. Menne, and R. Ruedy. 2024. “A NASA GISTEMPv4 Observational Uncertainty Ensemble.” *Journal of Geophysical Research: Atmospheres* 129, no. 17: e2023JD040179.

Lenssen, N. J., G. A. Schmidt, J. E. Hansen, et al. 2019. “Improvements in the GISTEMP Uncertainty Model.” *Journal of Geophysical Research: Atmospheres* 124, no. 12: 6307–6326.

MacCallum, S. N., and C. J. Merchant. 2011. “ARC-Lake v1.1 – Ancillary.” https://datashare.ed.ac.uk/handle/10283/132.

Menne, M. J., C. N. Williams, B. E. Gleason, J. J. Rennie, and J. H. Lawrimore. 2018. “The Global Historical Climatology Network Monthly Temperature Dataset, Version 4.” *Journal of Climate* 31, no. 24: 9835–9854.

Morice, C. P., J. J. Kennedy, N. A. Rayner, et al. 2021. “An Updated Assessment of Near-Surface Temperature Change From 1850: The HadCRUT5 Data Set.” *Journal of Geophysical Research: Atmospheres* 126, no. 3: e2019JD032361.

Polyakov, I. V., G. V. Alekseev, R. V. Bekryaev, et al. 2002. “Observationally Based Assessment of Polar Amplification of Global Warming.” *Geophysical Research Letters* 29, no. 18: 25–1.

Rohde, R. A., and Z. Hausfather. 2020. “The Berkeley Earth Land/Ocean Temperature Record.” *Earth System Science Data* 12, no. 4: 3469–3479.

Sippel, S., E. C. Kent, N. Meinshausen, et al. 2024. “Early-Twentieth-Century Cold Bias in Ocean Surface Temperature Observations.” *Nature* 635, no. 8039: 618–624.

Thompson, D. W., J. J. Kennedy, J. M. Wallace, and P. D. Jones. 2008. “A Large Discontinuity in the Mid-Twentieth Century in Observed Global-Mean Surface Temperature.” *Nature* 453, no. 7195: 646–649.

Titchner, H. A., and N. A. Rayner. 2014. “The Met Office Hadley Centre Sea Ice and Sea Surface Temperature Data Set, Version 2: 1. Sea Ice Concentrations.” *Journal of Geophysical Research: Atmospheres* 119, no. 6: 2864–2889.

Way, R. G., F. Oliva, and A. E. Viau. 2017. “Underestimated Warming of Northern Canada in the Berkeley Earth Temperature Product.” *International Journal of Climatology* 37, no. 4: 1746–1757.

Yin, X., B. Huang, M. Menne, et al. 2024. “NOAAGlobalTemp Version 6: An AI-Based Global Surface Temperature Dataset.” *Bulletin of the American Meteorological Society* 105, no. 11: E2184–E2193. https://doi.org/10.1175/BAMS-D-24-0012.1.

Zhang, H., B. Huang, J. Lawrimore, M. Menne, and T. Smith. 2020. “NOAA Global Surface Temperature Dataset (NOAAGlobalTemp).”